



Full length article

Crystallographic anisotropy of nonequilibrium solute capture

Xiao-Xiang Yu^{a,*}, John H. Perepezko^b, Laurence D. Marks^a

^a Department of Materials Science and Engineering, Northwestern University, Evanston, IL 60208, USA

^b Department of Materials Science and Engineering, University of Wisconsin-Madison, Madison, WI 53706, USA

ARTICLE INFO

Article history:

Received 28 February 2020

Revised 24 June 2020

Accepted 25 July 2020

Available online 31 July 2020

Keywords:

Nonequilibrium

Crystallographic anisotropy

Nickel-chromium alloy

High-temperature oxidation

Transmission electron microscopy

ABSTRACT

We demonstrate large, crystallographic anisotropy in nonequilibrium solute capture. Under identical conditions, differently oriented grains of a Ni-30Cr (wt.%) alloy were oxidized at 600°C for 60 s. For a Ni(Cr) (100) oriented grain, a solute captured rock salt oxide formed with a cube-cube epitaxial orientation. In contrast, for a Ni(Cr) (111) oriented grain, a solute captured corundum oxide formed with the (0001) basal plane parallel to (111). There are clear indications from the morphologies that are present – islands growing outwards for rock salt and islands growing inwards for corundum – that the oxide growth is dominated by kinetics, not thermodynamic factors. Since the interfacial conditions for nonequilibrium solute capture differ for cases where the metal/oxide boundary is moving (the (111) case) and where it is not (the (100) case), these results indicate that crystallographic anisotropy will have substantial effects which cannot be ignored in oxidation or corrosion.

© 2020 Acta Materialia Inc. Published by Elsevier Ltd. All rights reserved.

1. Introduction

Nickel-based superalloys are widely used due to their excellent combination of strength, ductility, and oxidation resistance at elevated temperatures [1]. Although there have been extensive studies on their oxidation and the dependencies on the composition, temperature, and oxygen pressure [2–5], much less work has focused on the microstructural factors of alloys such as grain size, grain boundaries, and crystallographic orientation. Besides, relatively few studies have combined a detailed analysis of the local chemistry and crystallography, and the present oxide phases have often been assumed to be thermodynamically stable. While equilibrium oxides are expected at a very long time, as we have recently pointed out [6], nonequilibrium oxides can readily form building upon the established science of nonequilibrium interfaces [7].

There are currently many unknowns with nonequilibrium solute capture. In addition to the original observations [6], further experimental data in both the gaseous oxidation and aqueous corrosion of nickel-chromium alloys has been reported [8–11], and it has been found in two other multicomponent alloys [12, 13]. While the thermodynamic conditions for Ni(Cr) alloys have been analyzed [14], the kinetics are only now starting to be examined in detail [15], and this is just for the simplified continuum models which do not include crystallographic anisotropy. To what extent

these nonequilibrium oxides depend upon the crystallographic anisotropy is still not understood.

In this note, we report that there is a considerable dependence upon the substrate crystallography of how nonequilibrium solute capture both initiates and develops with time. Using carefully-controlled pulse oxidation experiments where differently oriented Ni(Cr) alloy grains were oxidized under identical conditions, we find that a rock salt oxide grows outwards on (001) oriented grains, whereas a corundum oxide grows inwards on (111) oriented grains. Furthermore, there are clear indications of significant aging of the rock salt oxide, with partial precipitation of corundum inside the rock salt. For completeness, we are using the convention here, where “rock salt” corresponds to have a cation/anion arrangement similar to that in NaCl, and “corundum” identical to that in Al₂O₃, and not specifying the chemical composition which will be Ni_{1-x}Cr_xO_y where both *x* and *y* vary with the crystallography and how the oxide is formed.

Before describing the results, some background literature information on relevant crystallographic orientation effects in the oxidation of these alloys is appropriate; this provides some context, although there is no information in this literature as to the presence (or absence) of nonequilibrium phases. In general, the phases present were assumed to be simple, stoichiometric oxides and identified either from diffraction data or chemical analysis, it was not checked whether the composition in fact matched the assumptions. For the parent pure nickel, a significant dependence of the oxidation rate on crystallographic orientation has been found [16–23]. Nickel oxide films grown on Ni (111) surfaces were re-

* Corresponding author.

E-mail address: yuxx07@gmail.com (X.-X. Yu).

ported to have fewer grain boundaries than those grown on the Ni (100) surfaces. More recent studies have explored further the grain boundary distribution in NiO films formed on Ni single crystals with two orientations [24–26]. Oxides grown on the Ni (100) surface were reported to contain much higher fractions of high-angle grain boundaries than those grown on the Ni (111) surfaces. More grain boundaries, coupled with short-circuit diffusion, was invoked to explain the oxidation rate differences. Similar results have also been obtained for Ni-based alloys [27–29].

2. Experimental methods

A Ni-30Cr (wt.%) alloy was prepared from pure components (>99.99%) by arc melting. The sample was melted five times and flipped between each melt to ensure homogeneity. Following casting, the sample was homogenized for 120 h at 1200°C in a 4% hydrogen-argon atmosphere. In order to develop large grains of about 1 mm, the homogenized ingot was cold worked between 7–15%, then annealed at 1200°C for 120 h. Individual grain orientations were determined by electron backscattered diffraction (EBSD) in an FEI Quanta 650 scanning electron microscope (SEM). The EBSD samples were initially mechanically polished through successively finer grit sizes. For the final stage, electro-polishing was performed in the 2% (vol %) perchloric acid in a butoxyethanol electrolyte and 12V–15V direct current.

A pulse oxidation chamber was designed and built to conduct accurate, short-time oxidation experiments. The sample is supported on a cylindrical alumina crucible, which extends vertically into a quartz dome and is heated via induction coils that are placed around the dome at the height of the sample. During oxidation exposure, the chamber with the sample is initially evacuated. The chamber is then maintained under a flowing argon pressure of 5×10^{-4} torr while the sample is heated to the designated temperature. Once the temperature has stabilized, the gas is rapidly switched to the argon-oxygen gas mixture. Following the selected exposure, the sample is quenched by quickly turning back to flowing argon and shutting off the induction coil. For the experiments herein, the samples were oxidized at 600°C and a pressure of 5×10^{-4} torr (20% O₂ and 80% Ar) for 60 s. Of relevance later, we note that the thermal mass of the samples is small, so cooling is relatively rapid compared to the time for oxidation.

The transmission electron microscopy (TEM) samples were lifted out after the deposition of platinum protective layers on the oxidized surface in an FEI Helios Nanolab focused ion beam (FIB) instrument, and then thinned using the ion beam energy of 30 kV. A final cleaning step was performed at low energy (2 kV) to reduce the amorphous layer thickness. Atomic resolution scanning transmission electron microscopy (STEM) imaging was performed using an aberration-corrected JEOL ARM200CF microscope with collection angles β of $11 \text{ mrad} \leq \beta \leq 22 \text{ mrad}$ for the annular bright field (ABF) imaging and $90 \text{ mrad} \leq \beta \leq 220 \text{ mrad}$ for the high angle annular dark field (HAADF) imaging, these being acquired simultaneously. Chemical analysis was performed using a Gatan GIF electron energy loss spectrometer (EELS) and a dual silicon drift detector x-ray energy dispersive spectrometer (EDS) attached to the microscope.

3. Results

The macroscopic morphology of the oxide on the metal surface is shown in the secondary electron image at 30 kV by SEM in Fig. 1(a); there are significant differences in both the morphology and contrast of the oxide islands on Grain A and Grain B. We note that secondary electron images show contrast from atomic number (weak), topography (mainly with lower electron energies) and work function changes. The majority of the contrast differences in

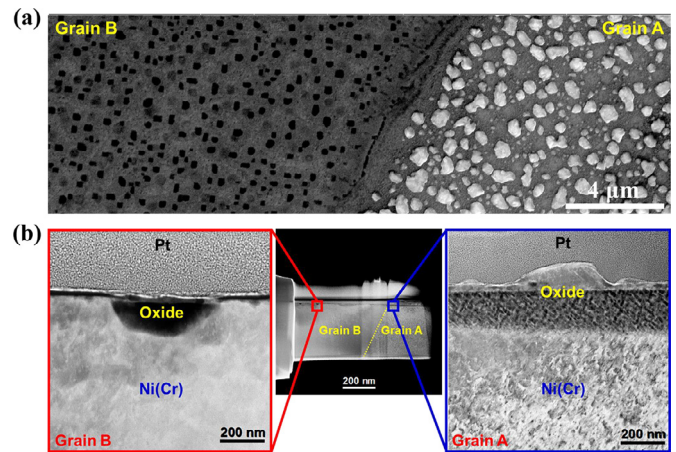


Fig. 1. (a) Secondary electron imaging in SEM at 30 kV showing the oxide islands grown on Grain A and Grain B with different morphologies. On the left, the oxide particles are dark; on the right, they are bright due to differences in work function, particularly in the flat regions between the islands. (b) Cross-sectional STEM-ADF images of the oxides on Grain A and B. Note that there is diffraction contrast in ADF images, hence the different intensities.

the oxides can be attributed to work function differences. Particularly in the regions between the islands where the oxide is somewhat flat. The cross-section STEM images, Fig. 1(b) from the same area, show that for Grain A, the oxide island grew outwards, and there is a thick oxide layer about 200 nm beneath the outer layer. For Grain B, however, the top oxide layer is much thinner (a couple of nanometers), and the oxide island grew inwards.

A detailed examination of Grain A in Fig. 2(a), for which the orientation is close to Ni(Cr) (100), shows that the top island is pure NiO and the thick oxide layer below consists of two phases. In Fig. 2(b), the bright contrast is the rock salt structure, and the dark contrast is the corundum structure in the HAADF-STEM image. Note that we are using the term “rock salt” to denote an oxide which has this specific crystallography, $Fm\bar{3}m$, but is not a simple composition; similarly our use of “corundum”, $R\bar{3}m$. The interface of the rock salt and corundum structure is coherent with the orientation relationship: rock salt (100)//corundum (0001), as shown in Fig. 2(c). Chemical analysis by EELS in Fig. 2(e) indicates about 15–20 at.% Cr was captured in the rock salt structure, and the corundum structure is nearly pure Cr₂O₃. The results suggest that the Cr₂O₃ phase precipitated in the rock salt matrix rather than forming a continuous sublayer, which is the consequence of nonequilibrium solute capture, as discussed elsewhere [6]. In other reported work on Ni(Cr) alloys (under different conditions), a spinel NiCr₂O₄ oxide phase has been observed [10, 30]. A thermodynamic analysis [14] indicates that the spinel has borderline stability, so it is not unreasonable that it will not be present in all cases.

For Grain B, where the orientation is close to Ni(Cr) (111), the corundum layer directly grew on the (111) surface as shown in Fig. 3(a), with the orientation relationship: Ni(Cr) (111)//corundum (0001), Fig. 3(b) and (e). The chemical line scanning in Fig. 3(c) shows only the bottom area of the inward island contains about 10 at.% Ni, while the top flat thin corundum layer in Fig. 3(d) is pure Cr₂O₃. The Cr₂O₃ thin film on the Ni(Cr) (111) grain is continuous without interfaces and boundaries compared to the oxide layer on the (100) grain.

To explore the initial states of different grain orientations, we checked the native oxide after electro-polishing the Ni(Cr) sample and storing it in the lab air for one week. The site-specific samples were FIB lifted out based on the EBSD mapping in Fig. 4(a). Two orientations (100) and (111) are compared, as shown in Fig. 4(b)

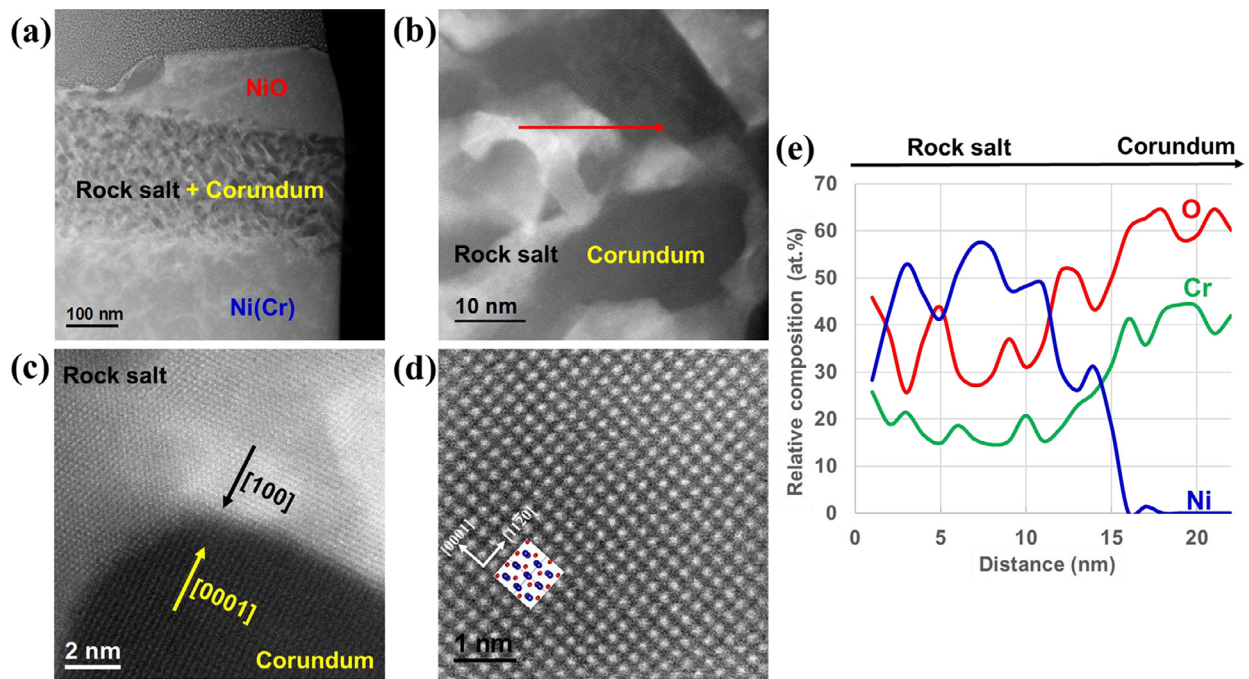


Fig. 2. Cross-sectional STEM-HAADF images for Grain A showing: (a) The outermost island is pure NiO and the thick oxide layer below consists of a mixture of rock salt and corundum phases. (b) Image from the two-phase region, showing bright contrast from the rock salt structure, and dark contrast from the corundum structure. (c) The orientation relationship between the rock salt and corundum structure is rock salt (100)//corundum (0001). (d) Atomic structure of the corundum phase. (e) Chemical analysis from an EELS scan for the red line marked in (b), in all cases normalized so to unity. The rock salt shows significant solute capture of Cr consistent with prior work [6].

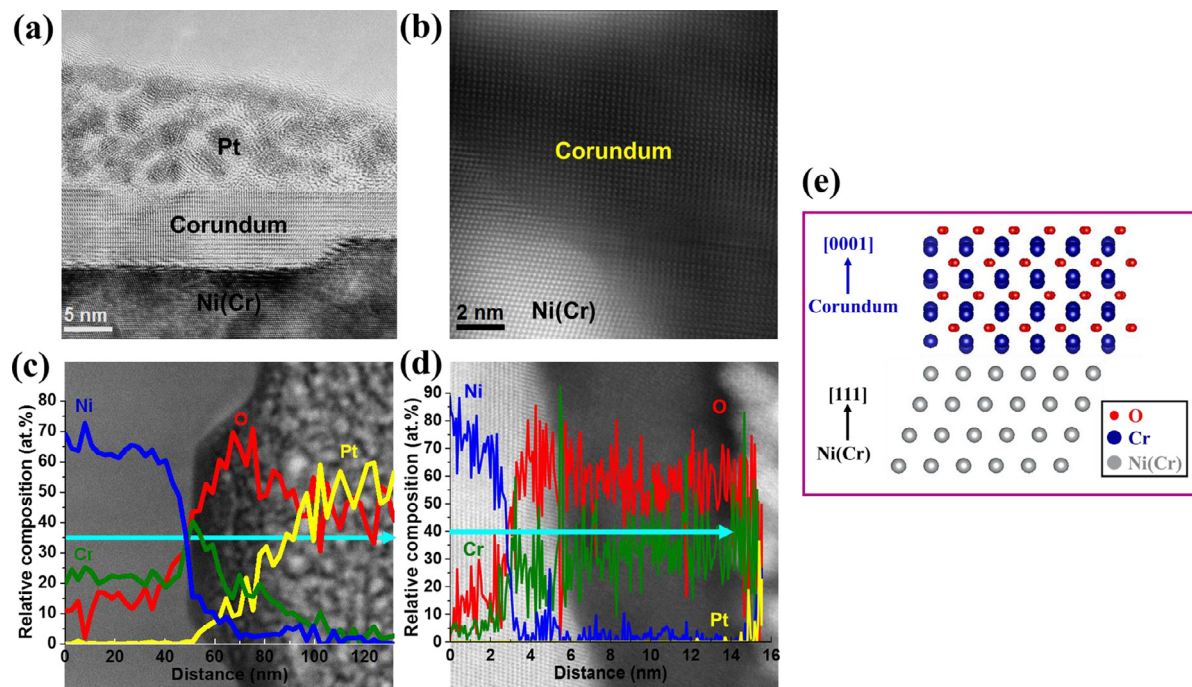


Fig. 3. Images for Grain B, (a) High-resolution TEM image showing the corundum layer and an inward growth island. (b) HAADF image of the corundum/metal interface. (c) An EDS line scan of the inner island superimposed on a lower magnification image, with Ni-rich regions near the alloy/oxide interface. (d) An EDS line scan of the top flat thin oxide film showing that it is close to pure Cr_2O_3 . (e) Illustration of the orientation relationship between the alloy and oxide, which is Ni(Cr) (111)//corundum (0001). Grey spheres for the alloy, blue for the cations, and red for the anions in the corundum structure.

and (c). For Ni(Cr) (111) grain, the native oxide is a corundum structure, and for Ni(Cr) (100) grain, the native oxide is rock salt. Moreover, although the native rock salt oxides grew epitaxially on the (100) surface, there are some misorientations between grains forming grain boundaries, as shown in Fig. 4(c).

4. Analysis

Some analysis is essential to understand why there are such significant differences in the oxides on the two grains. We need to expand upon three aspects: the shape of the oxide islands, why for

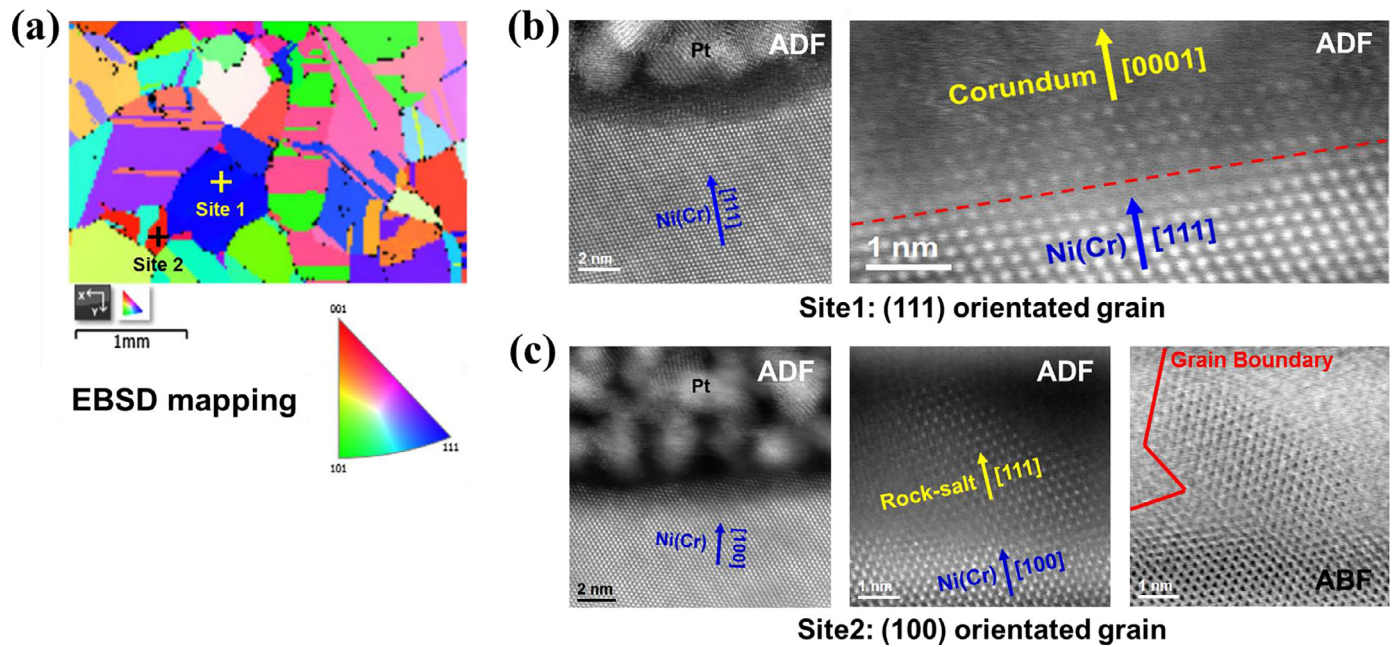


Fig. 4. The native oxides on Ni(Cr) (100) and (111) grains (a) EBSD map showing two regions marked from which FIB lift-out samples were prepared. (b) Site 1 is a (111) grain, and the native oxide is corundum structure, as shown by the ADF images. (c) Site 2 is a (100) grain, for which the native oxide is rock salt. Grain boundaries are labeled in the ABF image.

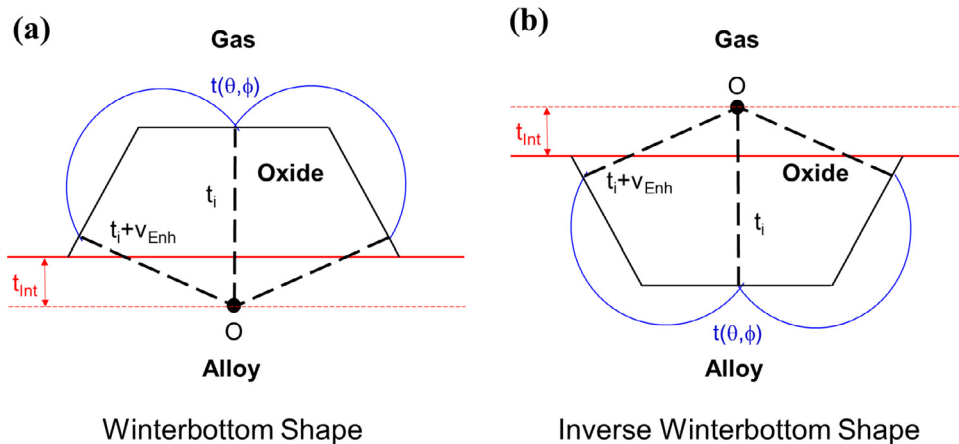


Fig. 5. Winterbottom shape in (a) and inverse Winterbottom shape in (b), with the Wulff center O marked in both. Both are minimum-energy thermodynamic or Lyapunov stable kinetic growth shapes. In both cases, one constructs an inner-envelope using the angular dependence $t(\theta, \phi)$, with the constraint that the outermost surface remains flat. As discussed in the text, the “ t ” terms are surface/interface free energies for thermodynamic control, surface/interface growth velocities for kinetic control.

rock salt oxide they are on top and inside the alloy for corundum, then how this connects to the aging of the nonequilibrium oxide. As we will see, the three are linked, and all point towards kinetic control of the phase and morphology rather than thermodynamic control.

For rock salt, the islands are the classical Winterbottom shape on top of the substrate [31], as illustrated in Fig. 5a, see also [32] and references therein. These are the thermodynamic or kinetic growth shapes for islands constrained to lie on a flat substrate and are standard in the Stranski–Krastanov (SK) mode or ‘layer-plus-island growth’ [33–35]. If thermodynamics control, the relevant terms are the interfacial free energies, and the parameter “ t_i ” in Fig. 5 is the surface free energy of the “ i ” facet in the ambient gas environment, “ t_{int} ” is the interface free energy and “ v_{Enh} ” (see below) is zero. (These terms can be generalized as weighted mean curvatures to include stress contributions [32, 36].) The constraint that the substrate remains flat can be violated if thermo-

dynamics dominate, in which case the particle will penetrate the substrate [37].

If the growth rate is fast compared to diffusion at the surface, one has kinetic control instead. In this case, the “ t_i ” are growth velocities of the different facets v_i , and “ t_{int} ” would be the growth rate into the alloy substrate. There can also be an additional term “ v_{Enh} ” since the activation energy barrier associated with the formation of a half-circular step terrace on a surface at the alloy/oxide/ambient triple point can be smaller than that to create a circular step terrace on a flat facet [32, 38]. We note that the rate of nucleation of step terraces has to be smaller than the growth rate of terraces as otherwise, one has rough surfaces as we recently analyzed for hydrothermal growth of KTAO_3 nanoparticles [39].

These Winterbottom shapes only depend upon interfacial growth velocities or chemical potentials; without loss of generality, the interfaces between the oxide and ambient in Fig. 5a can

be replaced by interfaces between the oxide and alloy, with the construction flipped as shown in Fig. 5b. The corundum islands, therefore, correspond to “inverse Winterbottom” shapes.

Which is important: thermodynamic or kinetic control? If thermodynamic control dominated for the corundum, it is unreasonable that the outermost oxide would remain flat, which implies that kinetic control dominates in this case. Growth occurs inwards since oxygen dominates diffusion in the corundum structure [40–42]. (We will return to the question of why corundum preferentially occurs on the (111) orientations in the discussion.)

By itself, the experimental morphology data does not uniquely determine whether the rock salt is growing under thermodynamic or kinetic control. However, cation vacancies dominate the diffusion in the rock salt structure [43, 44]. There are diffusive fluxes at the metal/alloy interfaces, but the interface is not in local equilibrium – if it was, there would be no solute capture. Since solute capture occurs when kinetics dominate, this strongly implies that the rock salt particles are growing outwards under kinetic control similar to the corundum growth inwards.

These interpretations are also consistent with the chemical composition of the oxide. In both cases (rock salt and corundum), the oxide adjacent to the metal formed most recently, that furthest is the oldest. The composition of the oxide near the interface is dominated by nonequilibrium solute capture, specifically the ratio of the effective growth velocity of the interface (including atomic fluxes crossing it) to an effective velocity for exchange of cations across the interface by a Zener diffusional process. Following Sherman et al. [14] and using the model of Aziz [45], the partition coefficient at the interface in the dilute limit is given by

$$k(\bar{V}) \equiv C^S/C^L = \frac{k_0 + \bar{V}}{1 + \bar{V}} \quad (1)$$

where C^S and C^L are the mole fractions of solute in the solid and liquid at the interface, k_0 is the equilibrium partition coefficient, \bar{V} is a nondimensionalized velocity defined as $\bar{V} = V\beta_0$ with $\beta_0 = a/D$ a characteristic inverse velocity from the ratio of a Zener hopping distance a , and the solute diffusivity across the interface D . The “velocity” term in Eq. (1) includes the relevant fluxes across the interfaces, i.e., for a planar interface in a binary alloy [46]

$$V(C - c^m) = j^o - J^M \quad (2)$$

Where V is the velocity normal to the interface that should be used in Eq. (1), C is the concentration of material transferred across the interface, c^m is the concentration in the metal, j^o is the flux across the oxide/metal interface and J^M is the flux in the metal at the interface. Taking as a reference an oxygen atom at the interface, which is stationary, for the (100) orientation, there is no oxygen flux, and the interface is with the dominant terms involving cation vacancies. In contrast, for the (111) case, the interface is moving, and there is no cation or metal flux. Thus, for the (100), the interfacial composition in the oxide is controlled by how rapidly the cations cross the interface versus exchange back with the metal (e.g., Cr and Ni swapping positions across the interface). For the (111), it is controlled by cation addition (probably by step-flow growth) at the interface versus (again) exchange across the interface. While there is solute capture for the (100) orientation and rock salt, as well as the (111) with corundum, the diffusing species are completely different. Thus, one has completely different magnitudes for the terms in Eqs. (1) and (2) for the two cases, in principle orders of magnitude different.

These nonequilibrium oxides are less stable than the standard oxides in phase diagrams, so with time, they will evolve, a process we will refer to as “aging” of the oxides. It is apparent that some aging is occurring during growth, and this aging is connected to the layered oxides commonly observed in extended oxidation studies.

The final piece to analyze is the transition from ‘layer-by-layer’ to three-dimensional islands, a morphological instability. This can occur due to thermodynamic criteria, for instance, stress relief or surface energy reduction, or correspond to kinetic control – a consequence of growth fluctuations. Since Wagner [47] formulated the criterion of metal/oxide interfacial stability when cations are the predominant diffusing species in oxides, many linear stability models [48–50] have been developed to determine the stability of a planar alloy/oxide interface. Based on those models [49, 50], instability occurs when the interdiffusion coefficient of the alloy is smaller than the diffusivity of oxygen in the oxide near the metal/oxide interface. However, this is inconsistent with our results: the diffusivity of Cr in Ni (diffusion coefficient at 600°C, $D_{Cr} \sim 5.9 \times 10^{-20}$ m²/s) [51] is larger than the diffusivity of oxygen in the corundum ($D_O \sim 9.3 \times 10^{-21}$ m²/s) [52].

Our results are instead consistent with kinetic control of the instability and the relevant diffusion constants: cation vacancies dominate the diffusion in the rock salt structure [43, 44], whereas oxygen dominates diffusion in the corundum structure [40–42]. The instability develops at whichever interface is growing most significantly – the outer for rock salt and the inner for corundum. What matters in our experiments are statistical fluctuations in the local growth rate, not diffusion at the interface. We note that, as mentioned earlier, if diffusional exchange across the interface was rapid, then one would not expect nonequilibrium solute capture.

5. Discussion

As we have discussed briefly in the introduction and further elsewhere [6, 13–15], it has frequently been assumed that thermodynamics dominate which oxide phases are formed during high-temperature oxidation and aqueous corrosion. Much of these assumptions were made where simultaneous crystal structure and chemical composition were not acquired, or the fine details could not be resolved. Of course, during high-temperature oxidation at very long time scales, the relative thermodynamics of the different oxide phases must dominate. Interestingly, during aqueous corrosion in steady-state, the passivating oxide thin films dissolve as rapidly as they grow, so equilibrium of phase and composition may never be reached.

Nonequilibrium solute capture has similarities to solute trapping by rapid solidification [7], but also significant differences. Solute trapping is usually active at temperatures close to the melting point where there is minimal crystallographic anisotropy in interfacial free energies. At the much lower temperatures where solute capture occurs, there will be substantial anisotropy. In addition, in solute trapping, diffusion in the liquid phase is very fast and probably dominates in all cases; in solute capture, all the diffusion is in the solid phase.

It is clear from the experimental data and analysis presented here that there is a vast richness in the differences that this leads to. Instead of simple addition to the solid surface in solute capture, now one has oxides growing either inwards or outwards depending upon which species preferentially diffuse. There is also apparent anisotropy associated with which phase nucleates – rock salt on Ni(Cr) (001) and corundum on Ni(Cr) (111). To understand this, note that both types of oxides contain close-packed oxygen planes, with the (0001) plane of corundum oxygen-terminated, whereas the (111) plane of rock salt is oxygen terminated. When the Ni(Cr) is (111) oriented, there will be a competition between nucleation of corundum and rock salt; the evidence indicates that the corundum wins. We note from Fig. 3(e) that there are indications that this is a low-energy interface. In contrast, there is no simple epitaxial relationship with a low misfit for the Ni(Cr) (001) orientation for corundum, which is consistent with preferable nucleation of the rock salt phase.

Even more complicated is the significant difference in the solute capture for the two phases, as well as the aging behavior. We will not speculate here upon the exact source of these, leaving this to future work. We strongly suspect that there is extensive interesting science yet to be determined in understanding how these nonequilibrium oxides evolve with time.

6. Conclusions

In this paper, it has been shown that grain orientation has a remarkable impact on nonequilibrium solute capture. Differences in macroscopic growth velocity with orientation, as discussed in the introduction, do not capture all the details; far more is taking place. It is clearly not correct to assume that continuous, pure NiO and Cr₂O₃ thin film form successively in Ni(Cr) alloys without grain orientation dependence [2–5]. Instead, as a function of crystallography, either nonequilibrium corundum forms first followed by inwards oxidation, or nonequilibrium rock salt forms first, and then a corundum phase initiates at the oxide/alloy interface.

Declaration of Competing Interest

The authors declare that they have no known competing financial interests or personal relationships that could have appeared to influence the work reported in this paper.

Acknowledgments

This work was supported by ONR MURI “Understanding Atomic Scale Structure in Four Dimensions to Design and Control Corrosion Resistant Alloys” on Grant Number N00014-16-1-2280. We thank Prof. Peter W. Voorhees for useful discussions and Mr. Evan J. Zeitchick for assistance with sample preparation.

References

- [1] T.M. Pollock, S. Tin, Nickel-based superalloys for advanced turbine engines: Chemistry, microstructure, and properties, *J. Propul. Power* 22 (2) (2006) 361–374.
- [2] D.L. Douglass, The oxidation mechanism of dilute Ni-Cr alloys, *Corros. Sci.* 8 (9) (1968) 665–678.
- [3] C. Giggins, F. Pettit, Oxidation of Ni-Cr-Al Alloys Between 1000 and 1200 C, *J. Electrochem. Soc.* 118 (11) (1971) 1782–1790.
- [4] B. Kear, F. Pettit, D. Fornwalt, L. Lemaire, On the transient oxidation of a Ni-15Cr-6Al alloy, *Oxidat. Metals* 3 (6) (1971) 557–569.
- [5] H. Hindam, D.P. Whittle, Microstructure, adhesion and growth-kinetics of protective scales on metals and alloys, *Oxidat. Metals* 18 (5-6) (1982) 245–284.
- [6] X.X. Yu, A. Gulec, Q. Sherman, K.L. Cwalina, J.R. Scully, J.H. Perepezko, P.W. Voorhees, L.D. Marks, Nonequilibrium solute capture in passivating oxide films, *Phys. Rev. Lett.* 121 (14) (2018) 145701.
- [7] J.C. Baker, J.W. Cahn, Solute Trapping by Rapid Solidification, *Acta Metall. Mater* 17 (5) (1969) 575–578.
- [8] X.X. Yu, A. Gulec, K.L. Cwalina, J.R. Scully, L.D. Marks, New insights on the role of chloride during the onset of local corrosion: TEM, APT, Surface Energy, and morphological instability, *Corrosion-Us* 75 (6) (2019) 616–627.
- [9] K.L. Cwalina, H.M. Ha, N. Ott, P. Reinke, N. Birbilis, J.R. Scully, In Operando Analysis of Passive Film Growth on Ni-Cr and Ni-Cr-Mo alloys in chloride solutions, *J. Electrochem. Soc.* 166 (11) (2019) C3241–C3253.
- [10] X.X. Yu, A. Gulec, C.M. Andolina, E.J. Zeitchick, K. Gusieva, J.C. Yang, J.R. Scully, J.H. Perepezko, L.D. Marks, In Situ observations of early stage oxidation of Ni-Cr and Ni-Cr-Mo Alloys, *Corrosion-Us* 74 (9) (2018) 939–946.
- [11] K. Lutton Cwalina, C.R. Demarest, A.Y. Gerard, J.R. Scully, Revisiting the effects of molybdenum and tungsten alloying on corrosion behavior of nickel-chromium alloys in aqueous corrosion, *Current Opin. Solid State Mater. Sci.* 23 (3) (2019) 129–141.
- [12] K.F. Quiambao, S.J. McDonnell, D.K. Schreiber, A.Y. Gerard, K.M. Freedy, P. Lu, J.E. Saal, G.S. Frankel, J.R. Scully, Passivation of a corrosion resistant high entropy alloy in non-oxidizing sulfate solutions, *Acta Mater* 164 (2019) 362–376.
- [13] X.X. Yu, M.A. Taylor, J.H. Perepezko, L.D. Marks, Competition between thermodynamics, kinetics and growth mode in the early-stage oxidation of an equimolar CoCrFeNi alloy, *Acta Materialia* 196 (2020) 651–659.
- [14] Q.C. Sherman, P.W. Voorhees, L.D. Marks, Thermodynamics of solute capture during the oxidation of multicomponent metals, *Acta Mater* 181 (2019) 584–594.
- [15] R. Ramanathan, P.W. Voorhees, Kinetics of solute capture during the oxidation of a multicomponent alloy, *Preparation* (2020).
- [16] J. Cathcart, G. Petersen, C. Sparks, The structure of thin oxide films formed on nickel crystals, *J. Electrochem. Soc.* 116 (5) (1969) 664–668.
- [17] R. Herchl, N. Khoi, T. Homma, W. Smeltzer, Short-circuit diffusion in the growth of nickel oxide scales on nickel crystal faces, *Oxidat. Metals* 4 (1) (1972) 35–49.
- [18] M. Graham, R. Hussey, M. Cohen, Influence of oxide structure on the oxidation rate of nickel single crystals, *J. Electrochem. Soc.* 120 (11) (1973) 1523–1529.
- [19] N.N. Khoi, W.W. Smeltzer, J.D. Embury, Growth and structure of nickel-oxide on nickel crystal faces, *J. Electrochem. Soc.* 122 (11) (1975) 1495–1503.
- [20] F. Czerwinski, J.A. Szpunar, The influence of crystallographic orientation of nickel surface on oxidation inhibition by ceria coatings, *Acta Mater* 46 (4) (1998) 1403–1417.
- [21] R. Peraldi, D. Monceau, B. Pieraggi, Correlations between growth kinetics and microstructure for scales formed by high-temperature oxidation of pure nickel. I. Morphologies and microstructures, *Oxidat. Metals* 58 (3-4) (2002) 249–273.
- [22] R. Peraldi, D. Monceau, B. Pieraggi, Correlations between growth kinetics and microstructure for scales formed by high-temperature oxidation of pure nickel. II. Growth kinetics, *Oxidat. Metals* 58 (3-4) (2002) 275–295.
- [23] L.P. Bonfrisco, M. Frary, Effects of crystallographic orientation on the early stages of oxidation in nickel and chromium, *J. Mater. Sci.* 45 (6) (2010) 1663–1671.
- [24] F. Czerwinski, A. Zhilyaev, J.A. Szpunar, Grain boundary character distribution in oxides formed on (100) and (111) nickel single crystals coated with ceria gel, *Corros. Sci.* 41 (9) (1999) 1703–1713.
- [25] H.L. Li, F. Czerwinski, J.A. Szpunar, The role of oxide grain boundary character distribution in nickel oxidation kinetics, defect and diffusion forum, *Trans. Tech. Publ.* (2001) 1683–1688.
- [26] H. Li, F. Czerwinski, A. Zhilyaev, J.A. Szpunar, Computer modelling the diffusion of Ni in NiO at high temperatures, *Corros. Sci.* 39 (7) (1997) 1211–1219.
- [27] F.H. Yuan, E.H. Han, C.Y. Jo, T.F. Li, Z.Q. Hu, The effect of crystallographic orientation on the oxidation behavior of a single-crystal nickel-base superalloy, *Oxidat. Metals* 60 (3-4) (2003) 211–224.
- [28] X. Wang, J.A. Szpunar, L.N. Zhang, Effect of surface crystallographic orientation on the oxidation behavior of Ni-based alloy, *Appl. Surf. Sci.* 327 (2015) 532–536.
- [29] X. Wang, F. Fan, J.A. Szpunar, L. Zhang, Influence of grain orientation on the incipient oxidation behavior of Haynes 230 at 900°C, *Mater. Character.* 107 (2015) 33–42.
- [30] L. Luo, L. Zou, D.K. Schreiber, D.R. Baer, S.M. Brummer, G. Zhou, C.-M. Wang, In-situ transmission electron microscopy study of surface oxidation for Ni-10Cr and Ni-20Cr alloys, *Scripta Mater.* 114 (2016) 129–132.
- [31] W.L. Winterbottom, Equilibrium Shape of a Small Particle in Contact with a Foreign Substrate, *Acta Metall. Mater* 15 (2) (1967) 303–310.
- [32] L.D. Marks, L. Peng, Nanoparticle shape, thermodynamics and kinetics, *J. Phys. Condens. Matter* 28 (5) (2016) 053001.
- [33] A. Pimpinelli, J. Villain, *Physics of Crystal Growth*, Cambridge University Press, Cambridge, U, 1999.
- [34] J. Venables, *Introduction to Surface and Thin Film Processes*, Cambridge University Press, 2000.
- [35] K. Oura, V. Lifshits, A. Saranin, A. Zotov, M. Katayama, *Surface science: an introduction*, Springer Science & Business Media, 2013.
- [36] J.E. Taylor, Mean-Curvature and Weighted Mean-Curvature. 2., *Acta Metallurg. Et Mater.* 40 (7) (1992) 1475–1485.
- [37] P.M. Ajayan, L.D. Marks, Evidence for sinking of small particles into substrates and implications for heterogeneous catalysis, *Nature* 338 (6211) (1989) 139–141.
- [38] E. Ringe, R.P. Van Duyne, L.D. Marks, Kinetic and Thermodynamic Modified Wulff constructions for twinned nanoparticles, *J. Phys. Chem. C* 117 (31) (2013) 15859–15870.
- [39] T. Ly, J. Wen, L.D. Marks, Kinetic growth regimes of hydrothermally synthesized potassium tantalate nanoparticles, *Nano Lett.* 18 (8) (2018) 5186–5191.
- [40] X. Ledoux, S. Mathieu, M. Vilasi, Y. Wouters, P. Del-Gallo, M. Wagner, Oxide Growth Characterization During Short-Time Oxidation of a Commercially Available Chromia-Forming Alloy (HR-120) in Air at 1,050 degrees C, *Oxidat. Metals* 80 (1-2) (2013) 25–35.
- [41] A.C.S. Sabioni, E.A. Malheiros, V. Ji, F. Jomard, W.A.D. Macedo, P.L. Gasteloi, Ion Diffusion Study in the Oxide Layers Due to Oxidation of AISI 439 Ferritic Stainless Steel, *Oxidat. Metals* 81 (3-4) (2014) 407–419.
- [42] S. Voyshnis, A. Seyeux, S. Zanna, B. Martin-Cabanas, T. Couvant, P. Marcus, Oxide layer growth on nickel-base alloy surfaces in high temperature water and in O₂ studied by ToF-SIMS with isotopic tracers, *Corros. Sci.* 145 (2018) 212–219.
- [43] M. O’Keeffe, W.J. Moore, Diffusion of oxygen in single crystals of nickel oxide, *J. Phys. Chem.* 65 (8) (1961) 1438–1439.
- [44] A. Atkinson, R. Taylor, The self-diffusion of Ni in NiO and its relevance to the oxidation of Ni, *J. Mater. Sci.* 13 (2) (1978) 427–432.
- [45] M.J. Aziz, Model for Solute Redistribution during Rapid Solidification, *J. Appl. Phys.* 53 (2) (1982) 1158–1168.
- [46] M.E. Gurtin, P.W. Voorhees, The thermodynamics of evolving interfaces far from equilibrium, *Acta Mater* 44 (1) (1996) 235–247.
- [47] C. Wagner, Oxidation of Alloys Involving Noble Metals, *J. Electrochem. Soc.* 103 (10) (1956) 571–580.
- [48] D. Whittle, D. Young, W. Smeltzer, The criterion for stability of a planar alloy-oxide interface upon oxidation of binary alloys, *J. Electrochem. Soc.* 123 (7) (1976) 1073–1079.

- [49] M.X. Zhang, Y.A. Chang, Stability of an Alloy oxide interface with oxygen ions being the dominant diffusing species in the oxide scale, *Acta Metallurg. Et Mater.* 41 (3) (1993) 739–746.
- [50] M. Bobeth, W. Pompe, M. Rockstroh, E. Schumann, Morphological instability of a planar oxide-alloy interface for inward oxide-growth, *Acta Metallurg. Et Mater.* 42 (2) (1994) 579–588.
- [51] S.P. Murarka, R.P. Agarwala, M.S. Anand, Diffusion of chromium in Nickel, *J. Appl. Phys.* 35 (4) (1964) 1339.
- [52] F. Lebreau, M.M. Islam, B. Diawara, P. Marcus, Structural, magnetic, electronic, defect, and diffusion properties of Cr₂O₃: A DFT+U Study, *J. Phys. Chem. C* 118 (31) (2014) 18133–18145.